2023 IEEE International Conference on Robotics and Automation (ICRA 2023)
May 29 - June 2, 2023. London, UK

Pose-graph SLAM Using Multi-order Ultrasonic Echoes and Beamforming for Long-range Inspection Robots

Othmane-Latif Ouabi[1], Neil Zeghidour[2], Nico F. Declercq[1,3], Matthieu Geist[2], Cédric Pradalier[1]

***Abstract*— This paper presents a Graph-based Simultaneous Localization And Mapping (GraphSLAM) approach for a robotic system relying on the reflections of ultrasonic guided waves to enable long-range inspection tasks on plate-based metal structures. A measurement model that can leverage multi-order acoustic echoes is introduced for accurate localization, and beamforming is used for mapping the boundaries of individual metal panels. These two elements are subsequently integrated within a nonlinear least squares optimizer to solve the full offline SLAM problem. We experimentally evaluate the potential of this approach in a laboratory environment. We observe the improved localization accuracy of the multi-order echo model compared to a second model, from previous works, that relies solely on first-order echoes. We also show that the proposed approach can yield accurate SLAM results, hence showcasing the standalone capability of ultrasonic-based GraphSLAM for envisioned long-range inspection applications.**

I. INTRODUCTION

Acoustic Simultaneous Localization And Mapping (acoustic SLAM) is a significant challenge that requires efficient solutions to allow for robotic inspection of large plate-based structures. A promising application is the long-range detection and localization of corrosion patches on large structures made out of metal panels assembled together, such as ship hulls and storage tanks (Fig.1, left). Indeed, when combined with other systems (inertial measurement unit, laser range-finder, ultra-wideband beacons...), Ultrasonic Guided Waves (UGWs) have the potential to provide accurate robot position, which is critical to inspection results obtained via acoustic imaging techniques [1]. In this context, UGWs may be useful for mapping the edges of the individual metal panels, as they can serve as structure-bound landmarks for localization, prior to a defect detection step.

On metal plates, guided waves can be generated by applying piezoelectric transducers in contact with the surface. These waves propagate radially around the emitter through the plate material, and potentially over large distances. When encountering the plate edges, these waves can be reflected, and a receiver can collect the acoustic echoes. As UGWs are also sensitive to material integrity [2], the resulting acoustic measurements carry essential information on the acoustic source position, the plate geometry, and the structure health.

[1]Othmane-Latif Ouabi, Nico F. Declercq and Cédric Pradalier are with GeorgiaTech Lorraine and the IRL2958 GT-CNRS in Metz, France. firstname.lastname@georgiatech-metz.fr

[2]Neil Zeghidour and Matthieu Geist are with Google Research, Brain Team. {neilz, mfgeist}@google.com

[3]Nico F. Declercq is also with Georgia Institute of Technology, Atlanta, GA 30332-0250, USA. declercq@gatech.edu

This work is part of the BugWright2 project. This project was supported by the European Commission under grant agreement 871260 - BugWright2.

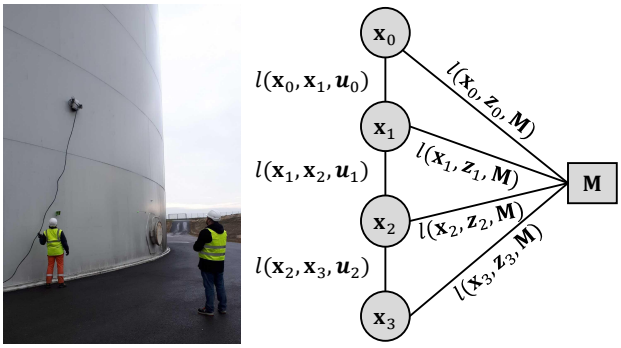

Fig. 1: Left: Typical operation conditions of the Altiscan magnetic crawler on a storage tank. Right: Graph representation of the SLAM problem, where the variables to estimate are the positions $\mathbf{x}_i$ and the map $\mathbf{M}$, the inputs are the odometry data $\mathbf{u}_i$ and measurements $\mathbf{z}_i$, and the constraints between the variables are represented with the l functions.

In mobile robotics applications, SLAM is typically one of the most significant challenges to address. Solving the *full* SLAM problem usually involves high-dimensional batch optimization over a sparse graph, where the unknown variables (robot positions and map) are the nodes, and the edges between them represent information constraints that are induced either by odometry or measurements (Fig.1, right). Unlike online filtering techniques, such as Kalman filtering or particle filtering [3], GraphSLAM [4] can use the information contained in *all* the measurements to infer the target variables. In the context of long-range robotic inspection, we envision that GraphSLAM, through a complete optimization over all the measurements, may support accurate robot localization and structure geometry mapping. Nevertheless, applying GraphSLAM techniques to UGWs measurements is challenging due to the inherent complexity of the measurements that present wave dispersion effects [5] and multi-echoes characteristics [6].

This work presents an *offline* GraphSLAM approach to simultaneously recover the trajectory of an inspection robot along with individual metal plates geometry from odometry and ultrasonic measurements. Our setup only requires a single omnidirectional emitter/receiver sensor mounted on the mobile platform. We introduce an observation model that can leverage multi-order echoes for localization, and we rely on beamforming [7], a standard spatial filtering technique, to map the plate boundaries. These two elements are subsequently integrated within a Nonlinear Least Squares (NLS) optimizer to solve the full SLAM problem. We show experimentally, using ultrasonic measurements acquired in a

laboratory environment, that the proposed observation model leads to better localization accuracy when compared to a simpler first-order echo only model from previous works. Furthermore, we illustrate that the proposed GraphSLAM approach has potential to yield accurate SLAM results.

II. Related work

On the one hand, UGWs are usually deployed on sensor networks that are permanently attached to the structure for defect detection and localization using prior knowledge of the sensor positions [8], [2]. This setup, however, is restricted to monitor a minimal and fixed area. On the other hand, mobile robots can be deployed to perform point-by-point thickness measurements [9]. However, the overall inspection coverage is sparse, as only the surface beneath the probe is effectively controlled with a single measurement. The use of omnidirectional UGWs is a promising prospect to overcome the inherent limitations of the two mentioned setups [1], [10]. Yet, deploying long-range UGW-based techniques in practice on a mobile platform is still a significant challenge.

GraphSLAM is an approach that is now well studied [4]. Numerous GraphSLAM methods and solvers have been developed, with increasing computational efficiency [11], [12], [13]. These techniques have gained such maturity that they can seamlessly adapt to various sensor modalities (Laser, computer vision, IMU...) and SLAM problems. GraphSLAM can be applied to direct line-of-sight range measurements [14], [15], and has been used in combination with beamforming [16]. The integration of multi-path components has been investigated [17], but it leads to significant complexity due to the explicit data association problem.

In the literature, [18], [19], [20] attempt to achieve acoustic SLAM to simultaneously recover the geometry of a room along with the observation positions using acoustic echoes from the walls. Yet, they rely on the critical assumptions that only first-order echoes are detected, and assume that the echo-wall associations are flawlessly known. [21] does not rely on such assumptions, but the work is restricted to a simple (one-dimensional) case with linear transition and observation models. Closer to our case-study, UGWs measurements acquired with a single omnidirectional emitter/receiver have been integrated within a particle filter to achieve on-plate acoustic SLAM [22], [6]. Yet, these online filter-based methods do not leverage high-order acoustic echoes, whereas they contain crucial localization and mapping information.

Overall, an elegant solution to the *full* acoustic SLAM problem using a single omnidirectional emitter/receiver device, and leveraging multi-order signal reflections, is still lacking. We propose here a novel GraphSLAM approach to enable its emergence and application to inspection robots. Our approach builds on a custom multi-order measurement model along with beamforming. It has low complexity, as it does not require any echo-extraction step that would make it sensitive to echo detection errors, and would necessitate explicit echo-plate boundary association, which is a challenging task for ultrasonic measurements. The experimental results illustrate the potential of the proposed approach.

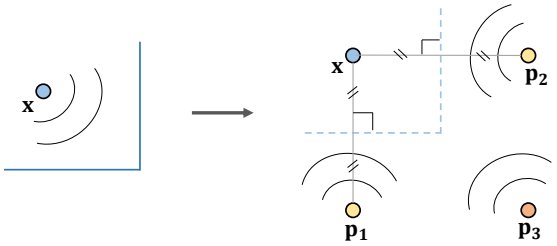

Fig. 2: Illustration of the image source principle. (Left) actual setup with an omnidirectional emitter/receiver in a partially bounded space. (Right) Equivalent setup provided by the image source model. The first-order image sources at $\mathbf{p}_1$ and $\mathbf{p}_2$ are obtained by symmetry of the real source on each boundary. The second-order one at $\mathbf{p}_3$ is obtained by symmetry of one of the first-order image sources.

III. Method

We consider a mobile platform equipped with an emitter/receiver pair of co-located contact acoustic sensors, and moving on a metal surface. At the i^{th} scanning position, the emitter at position $\mathbf{x}_i = [x_i, y_i, \alpha_i]^T$ (2D pose + orientation) sends an omnidirectional acoustic wave with a pulse $s(t)$ through the plate. Simultaneously, the receiver collects the acoustic response $z_i(t)$, which contains acoustic echoes due to reflections of the incident wave on plate boundaries. We assume that noisy odometry information $\mathbf{u}_i$ is available (typically provided by wheel encoders or an IMU). The objective is to infer both the full robot trajectory $\mathbf{x}_{0:T}$ and map $\mathbf{M}$ that accounts for the plate boundary positions. In this work, we do not consider other acoustic scatterers such as defects. However, their detection and localization shall be considered in future works for a complete inspection task.

A. Measurement model

The ultrasonic measurements essentially contain the successive reflections of the excited wave on plate boundaries. They can be modeled based on the image source model [23], which states that the reception of any edge reflection can be interpreted as a signal originating directly from a fictive image source. The image sources positions depend on the position of the actual emitter and map geometry, as illustrated in Fig 2. This results in the signal model:

$$z_i(t) = \sum_{\mathbf{p} \in \mathcal{I}(\mathbf{x}_i, \mathbf{M})} g(||\mathbf{p} - \mathbf{x}_i||, t) * s(t) + n_i(t),$$

where $\mathbf{x}_i$ is the robot position at time step i, $||.||$ is the Euclidian norm in $\mathbb{R}^2$ calculated on the x, y coordinates only, $\mathcal{I}(\mathbf{x}_i, \mathbf{M})$ the set of the image sources positions for a plate geometry $\mathbf{M}$ and a real source position $\mathbf{x}_i$, $g(||\mathbf{p} - \mathbf{x}_i||, t)$ is the acoustic transfer function of the propagation medium, and $*$ denotes the convolution operation. With the assumption that the material is isotropic (*i.e* wave propagation is the same in any direction), the propagation transfer is only a function of time and of the distance between the receiver and the image source. $n_i(t)$ is an additive Gaussian noise term, that we assume temporally and spatially white.

B. Localization with a multi-order echo model

In the first step, we design an observation model that can leverage multi-order reflections from UGWs measurements for localization only on a metal panel. Following the procedure described in [6], we determine correlation signals, from the measurements, to assess the likelihood that a *single* acoustic reflection occurred at any distance r with:

$$z_i'(r) = \frac{\langle z_i(t), \hat{z}(r,t)\rangle}{\sqrt{\langle z_i(t), z_i(t)\rangle \langle \hat{z}(r,t), \hat{z}(r,t)\rangle}},$$

where $\hat{z}(r,t) = \hat{g}(2r,t) * s(t)$ is the expected signal containing an echo due to a reflection at a distance r, $\hat{g}$ is a propagation model as in [6], and $\langle .,. \rangle$ denotes the usual scalar product for time-continuous signals. We subsequently retrieve their envelope with $e_i(r) = |z_i'(r) + j\mathcal{H}(z_i')(r)|$, where $\mathcal{H}$ denotes the Hilbert transform operator.

Assuming a known plate geometry $\mathbf{M}$, we model, for a candidate sensor position $\mathbf{x}$, the expected envelope signal as a mixture of Gaussian functions:

$$\hat{e}(\mathbf{x}, r) = \sum_{\mathbf{p}\in\mathcal{I}(\mathbf{x},\mathbf{M})} \mu_{\mathbf{p}} \cdot \exp\left\{-\left(\frac{r - ||\mathbf{p}-\mathbf{x}||}{\sigma}\right)^2\right\},$$

where $\mathcal{I}(\mathbf{x},\mathbf{M})$ contains the image source positions, and σ is a positive parameter. As the amplitudes $\mu_{\mathbf{p}}$ are not known a priori, we propose to estimate them by minimization of the mean-squared error between $\hat{e}(\mathbf{x}, r)$ and $e_i(r)$. Let's first discretize the different variables: $\hat{\mathbf{e}}(\mathbf{x}) = [\hat{e}(\mathbf{x}, r_1), ..., \hat{e}(\mathbf{x}, r_M)]^T$ and $\mathbf{e}_i = [e_i(r_1), ..., e_i(r_M)]^T$, $M \in \mathbb{N}$. Let's define a "steering" vector function:

$$\mathbf{a}(\mathbf{x}, \mathbf{p}) = \left[\exp\left\{-\left(\frac{r_i - ||\mathbf{p}-\mathbf{x}||}{\sigma}\right)^2\right\}\right]^T_{1\le i\le M}.$$

Let's call $N(\mathbf{x},\mathbf{M})$ the number of image sources $\mathbf{p}_n$, $n = 1..N(\mathbf{x},\mathbf{M})$, in $\mathcal{I}(\mathbf{x},\mathbf{M})$ whose signal can be observed in $\mathbf{e}_i$, as they are such that $||\mathbf{p}_n - \mathbf{x}|| < r_M$. After definition of the $M \times N(\mathbf{x},\mathbf{M})$ dictionary matrix:

$$\mathbf{A}(\mathbf{x},\mathbf{M}) = \left[\mathbf{a}(\mathbf{x},\mathbf{p}_1), \mathbf{a}(\mathbf{x},\mathbf{p}_2), ..., \mathbf{a}(\mathbf{x},\mathbf{p}_{N(\mathbf{x},\mathbf{M})})\right],$$

the expected envelope measurement obtained for a candidate position $\mathbf{x}$ is defined as

$$\hat{\mathbf{e}}(\mathbf{x},\mathbf{M},\mathbf{e}_i) = \mathbf{A}(\mathbf{x},\mathbf{M}) \cdot \hat{\boldsymbol{\mu}}(\mathbf{x},\mathbf{M},\mathbf{e}_i), \qquad (1)$$

where $\hat{\boldsymbol{\mu}}(\mathbf{x},\mathbf{M},\mathbf{e}_i) \in \mathbb{R}^{N(\mathbf{x},\mathbf{M})}$ is the least square estimate:

$$\hat{\boldsymbol{\mu}}(\mathbf{x},\mathbf{M},\mathbf{e}_i) = \left[\mathbf{A}^T(\mathbf{x},\mathbf{M})\mathbf{A}(\mathbf{x},\mathbf{M})\right]^{-1}\mathbf{A}^T(\mathbf{x},\mathbf{M}) \cdot \mathbf{e}_i.$$

The positions of the image sources required to determine $\hat{\mathbf{e}}$ can be analytically derived for polygonal geometries based on the image source algorithm. For a rectangular panel with dimensions $w \times h$ and a source at $\mathbf{x} = [x, y]$ expressed in the plate frame as represented in Fig.3, we have [24]:

$$\mathcal{I}(\mathbf{x},\mathbf{M}) = \left\{[2nw \pm x, 2mh \pm y]^T / (n,m) \in \mathbb{Z}^2\right\} / (x,y).$$

In Fig. 4, we illustrate how the envelope signal model can adequately match the measurements. Fig. 4a shows an experimental ultrasonic measurement obtained on an aluminium plate in a laboratory environment. Fig. 4b shows the corresponding envelope signal obtained after correlation with a wave propagation model. It is superimposed with the expected envelope signal, which is calculated with Eq. (1) based on the ground-truth sensor position and plate size. It can be seen that there is a good match between the measured and expected envelopes, as there is an appropriate correspondence for all the positions of the local maxima.

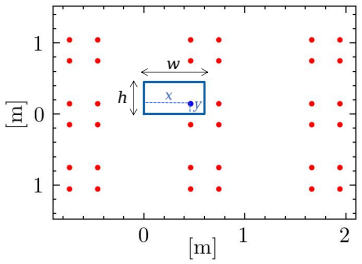

Fig. 3: Shows the positions of the image sources (red dots) for a rectangular plate (in blue) with dimensions $w \times h$, and a fixed emitter position $[x, y]$ (blue dot).

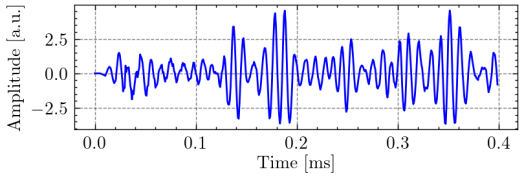

(a) An experimental ultrasonic measurement.

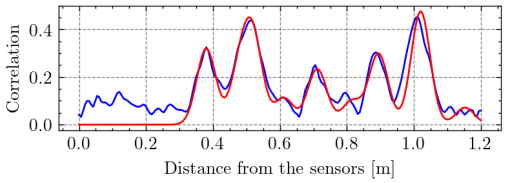

(b) The envelope signal obtained from (a) superimposed with the expected envelope (in red) after matching the model in Eq. (1) with the former. A value $\sigma = 2$cm is used.

Fig. 4: Illustration of the envelope signal obtained from an experimental ultrasonic measurement acquired on a rectangular metal panel, and comparison with the expected envelope calculated with the matched Gaussian mixture model.

Last, to localize the emitter/receiver on a metal panel given an envelope measurement $\mathbf{e}$, one may simply use the mean squared error between expected and measured envelope signals as a log-likelihood function of the sensor position:

$$l(\mathbf{x}|\mathbf{e}) \propto -||\hat{\mathbf{e}}(\mathbf{x},\mathbf{M},\mathbf{e}) - \mathbf{e}||^2.$$

The position of the maximum of this (highly non-linear) function yields a Maximum Likelihood (ML) position estimate. This will be further illustrated in the results section.

C. Mapping only via beamforming

To map the plate boundaries, we use a beamforming approach [6], that is briefly recalled here for completeness and adapted notations. The plate geometry is represented

by a set of lines: $\mathbf{M} = \{r_l, \theta_l\}_{l=1..4}$ where the parameters (r_l, θ_l) define the line equation in the 2D plane with $x \cdot \cos\theta_l + y \cdot \sin\theta_l - r_l = 0$ in a non-mobile frame with respect to the plate. Moreover, we limit our case-study to rectangular shapes, hence the potential geometries possess only four lines forming a rectangle altogether. This is not a significant limitation for inspection on ship hulls and storage tanks as they are, in the majority, made out of rectangular panels, as illustrated in Fig.1. With the assumption of a known sensor trajectory $\mathbf{x}_{0..T}$, we create the beamforming map with:

$$\mathcal{L}_{\mathbf{x}_{0:T}}(r, \theta) = \sum_{i=0}^{T} e_i(d_{\mathbf{x}_i}(r, \theta)),$$

where $d_{\mathbf{x}_i}(r, \theta) = 2 \times |x_i \cdot \cos\theta + y_i \cdot \sin\theta - r|$ is the distance between the sensor and the first-order image source related to a reflection of the excitation signal on an edge with coordinates (r, θ). It must be noted that, for mapping, only first-order reflections are taken into account in the model, as we reason on individual edges for computational efficiency. Next, we estimate the plate geometry with:

$$\hat{\mathbf{M}}(\mathbf{x}_{0:T}) = \arg\max_{\mathbf{M}} \sum_{(r,\theta)\in\mathbf{M}} \mathcal{L}_{\mathbf{x}_{0:T}}(r, \theta), \qquad (2)$$

where $\mathbf{M}$ is restricted to be a rectangle. This optimization problem can be solved efficiently by taking this constraint into account [6]. Although it is limited here to rectangular shapes, this mapping approach can be practically generalized to arbitrary 2D convex polygonal shapes by adding a regularization term to the cost in Eq. (2) [25].

D. Integration of beamforming within GraphSLAM

GraphSLAM aims at finding a maximum a posteriori estimate of the map and robot trajectory given odometry and ultrasonic measurements over the full posterior distribution. Under the assumption of Gaussian distribution of the measurements, this amounts to minimize the negative logarithm of the posterior distribution that we model as:

$$J(\mathbf{x}_{0:T}, \mathbf{M}) = \sum_{i=0}^{T-1} ||\mathbf{x}_{i+1} - f_{\text{dyn}}(\mathbf{x}_i, \mathbf{u}_i)||^2_{\mathbf{\Sigma}} + \lambda \cdot \sum_{i=0}^{T} ||\hat{\mathbf{e}}(\mathbf{x}_i, \mathbf{M}, \mathbf{e}_i) - \mathbf{e}_i||^2, \quad (3)$$

where $||.||_{\mathbf{\Sigma}}$ is the Mahalanobis distance with covariance matrix parameter $\mathbf{\Sigma}$, λ is a positive parameter used to balance the importance between odometry and ultrasonic measurements in the cost, and f_{dyn} is the transition model. One may note the convenience of such formulation, as it never requires the extraction of the individual echoes contained within the measurements, or their association with the unknown boundaries they would originate from.

Within this optimization formulation, we propose to integrate beamforming, as it can reliably infer the map $\mathbf{M}$ given a trajectory, and thus provide relevant map initialization, which can be critical when relying on iterative NLS optimizers. This integration is achieved by minimizing $\tilde{J}(\mathbf{x}_{0:T}) \triangleq J(\mathbf{x}_{0:T}, \hat{\mathbf{M}}(\mathbf{x}_{0:T}))$, where $\hat{\mathbf{M}}(\mathbf{x}_{0:T})$ is as in Eq. 2, hence reducing the dimensionality of the problem.

Assuming that a "good" initial guess of $\mathbf{x}_{0:T}$ is available, the minimization of $\tilde{J}$ is achieved using the standard NLS approach [4]. Yet, due to the integration of beamforming, the Jacobian of the residuals $\mathbf{E}$, defined such that $\tilde{J}(\mathbf{x}_{0:T}) = \mathbf{E}^T(\mathbf{x}_{0:T})\mathbf{E}(\mathbf{x}_{0:T})$, is not sparse. Indeed, all the terms in the second sum in Eq. (3) depend on the full trajectory when $\mathbf{M} = \hat{\mathbf{M}}(\mathbf{x}_{0:T})$. Even tough we are addressing the offline SLAM problem, this approach would not be scalable to large trajectories due to the extensive computational time.

To remedy that, we assume that the map does not vary with infinitesimal variations of the trajectory. Under this assumption, the Jacobian matrix of $\mathbf{E}$ is sparse, and can be efficiently calculated [26]. Overall, for each iteration of the optimization process, we first update the trajectory with a NLS step. Next, the map is determined via beamforming with Eq. (2). This two-steps process is then repeated until the variation of the loss becomes lower than a threshold.

IV. Experiments

We assess the efficiency of our GraphSLAM approach on two sets of acoustic measurements acquired on two rectangular metal panels, in a laboratory environment. The first plate is in aluminium and has dimensions 600x450x6mm (Scenario 1), while the second plate is in steel and has dimensions 1700x1000x6mm (Scenario 2). The measurements are acquired by manually placing an emitter/receiver pair of co-located transducers at well-defined locations. Further details on the acquisition procedure are available in [6].

A. Evaluation of the multi-order echo observation model

To assess the benefit of using a multi-order echo observation model for localization, we first compare the localization accuracy achieved both with the proposed model, and with a simpler observation model used in [6], that only relies on first-order reflections. To this aim, given an envelope measurement $\mathbf{e}_i$, we model the log-likelihood of the sensor presence at any position $\mathbf{x}$ with:

$$l_{1^{\text{st}}\text{order}}(\mathbf{x}|\mathbf{e}_i) = \sum_{(r,\theta)\in\mathbf{M}} e_i(d_{\mathbf{x}_i}(r, \theta))$$

for the first-order model, and with:

$$l_{\text{multi-order}}(\mathbf{x}|\mathbf{e}_i) = -||\hat{\mathbf{e}}(\mathbf{x}, \mathbf{M}, \mathbf{e}_i) - \mathbf{e}_i||^2$$

for the multi-order echo model. We determine likelihood maps for each model, using different envelope measurements $\mathbf{e}_i$, and based on the known plate geometry $\mathbf{M}$. A likelihood maximum is expected at the true sensor position. We show, in Fig. 5, several instances of likelihood maps obtained for each model, with the aim to illustrate the likelihood patterns obtained from the measurements acquired on the two metal panels. One may notice that the likelihood maps present the same two axis symmetries than the rectangular plates due to the ambiguity of the echo (range-only) measurements, which cannot be disambiguated without the integration of an external localization system.

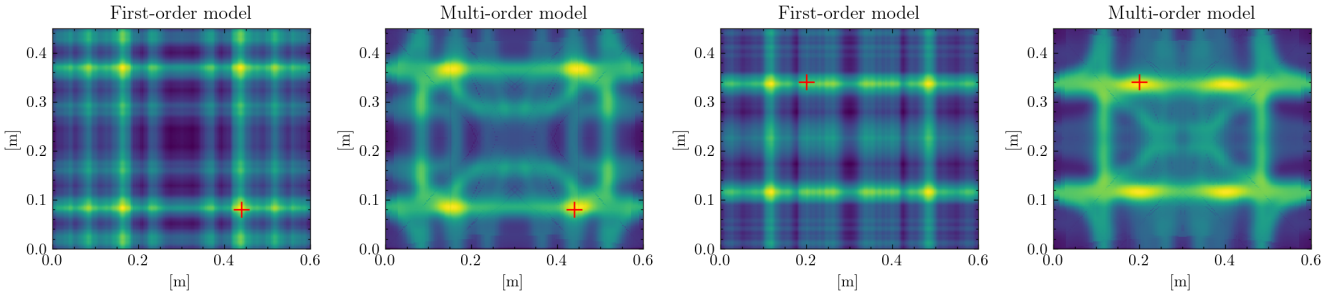

(a) Correct localization for the two models.

(b) Correct localization for the multi-order model only.

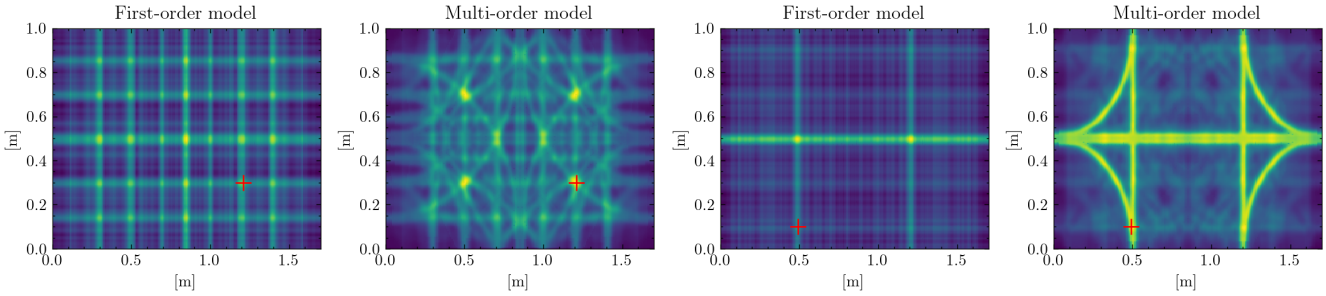

(c) Correct localization for the multi-order model only.

(d) Typical effect induced by overfitting of the multi-order model.

Fig. 5: Likelihood maps of sensor presence obtained using measurements acquired on the aluminium plate (a), (b), and on the steel plate (c), (d). The true sensor position is indicated by the red mark. The outline of each plot accounts for the plate boundaries, and the color maps only spans the range from the minimum to the maximum likelihood value.

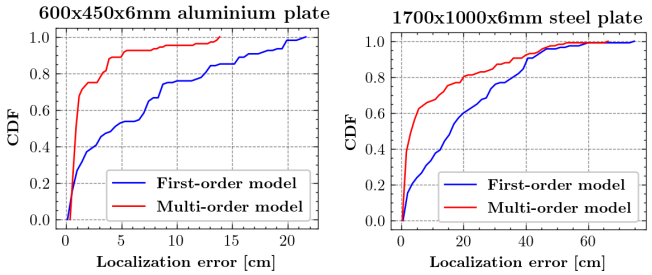

Fig. 6: Empirical Cumulative Distribution Functions (CDF) of the localization error obtained with the ML position estimates in the two scenarios under consideration.

We first qualitatively assess the performance of the observation models. Fig. 5a depicts a scenario where the two models point to the correct sensor position. In Fig.5b, only the first-order model does not point to the correct sensor position. This is due to signal interference. Namely, one energetic reflection in the envelope measurement is erroneously "interpreted" by the model as a reflection originating from an incorrect boundary (the left one in this case), leading to poor localization accuracy. Furthermore, highly energetic high-order reflections also contribute to localization errors, because the model can possibly interpret them as first-order ones. With the multi-order echo model, however, a likelihood maximum can be identified at a much closer location to the ground truth sensor position. The same observations hold for Fig. 5c, which depicts the likelihood maps for one measurement acquired on the large steel plate. This illustrates that the multi-order approach is better suited for localization. Fig. 5d illustrates the detrimental effect caused by "overfitting" of the multi-echo model, which occurs when the correlation value due to one reflection is relatively important compared to the other ones in the measurement. Indeed, due to the estimation of the coefficients $\mu_{\mathbf{p}}$ in Eq. III-B through matching the expected and measured envelope signals, the former will present substantial similarity with the measurement for any candidate sensor position for which the echo is expected (either as a first or a high-order echo). This results in higher localization ambiguity. Yet, this phenomenon is observable in the dataset for only a very limited number of measurements. We will see later whether the proposed GraphSLAM approach can yield accurate results in their presence.

With the aim to quantitatively compare the model's performances, we evaluate the empirical cumulative distributions of the localization error obtained with the ML position estimates for the two datasets. As the localization ambiguity due to the plate symmetries cannot be resolved when relying solely on UGWs, we only consider a single quarter of the plate when we determine the ML estimates, and evaluate its minimum distance to the 4 symmetrical points of the truth position.

We show in Fig. 6 the empirical distributions obtained for each of the two models, and in the two scenarios. One can observe that in the first one, the localization error is lower than 2cm for 75% of the data when relying on the multi-order model, and the median error is 0.8cm. To reach the same proportion with the first-order model, the error must be higher than 10cm, and the median error is 4cm. In the second scenario, the localization errors are relatively higher. This could be due to lower signal-to-noise ratio and larger plate surface. Still, the multi-order model clearly outperforms the first-order model in localization accuracy. For example, the

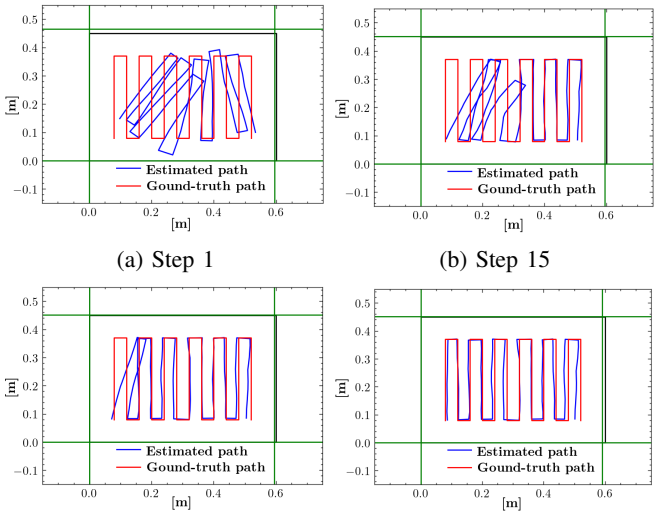

(a) Step 1 (b) Step 15

(c) Step 29 (d) Step 41

Fig. 7: Representation of the SLAM results during iteration steps 1, 15, 29, and 41 of the NLS optimization process using the data from Scenario 1. The true outline of the plate is represented by the black rectangle. The reconstructed (resp. ground truth) trajectory is represented in the estimated (resp. ground truth) plate frame for easier comparison.

median localization errors are respectively 3cm and 15cm.

Overall, these results support the benefit of using our approach that can leverage multi-order echoes for localization, compared to a first-order echo only model.

B. Experimental localization and mapping results

In the following, we evaluate the performance of the proposed GraphSLAM approach that integrates the multi-order observation model. We simulate "lawn mower" trajectories for the two scenarios by using the theoretic displacement between the truth measurement positions as noise-free odometry, and add Gaussian noise to the displacement data. The resulting dead-reckoning trajectory is then used for initialization of the NLS optimizer. We first run the optimizer using the data from Scenario 1. We represent, in Fig. 7, the qualitative SLAM results obtained at different steps of the optimization process. One can observe that the dead-reckoning trajectory, shown in Fig. 7a, presents noticeable drift. Yet, the plate dimensions are well recovered, which illustrates the robustness of beamforming to localization

Scenario	Optimization step	Loc. error [cm]	Map. error [cm]
1	Initial	4.50 ± 0.63	1.42 ± 0.92
	Final	1.14 ± 0.76	0.46 ± 0.06
2	Initial	5.09 ± 0.52	2.31 ± 1.43
	Final	2.37 ± 0.45	1.61 ± 0.24

TABLE I: Means and standard deviations of the localization and mapping errors in the two scenarios. These are calculated over 10 repetitions of the optimization process, after randomly sampling the (simulated) noisy odometry data.

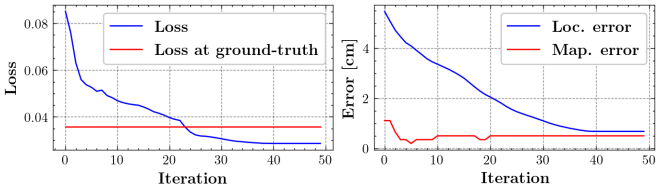

Fig. 8: Evolution of the GraphSLAM cost (left), the localization and mapping errors (right) during the NLS optimization when using the data from Scenario 1.

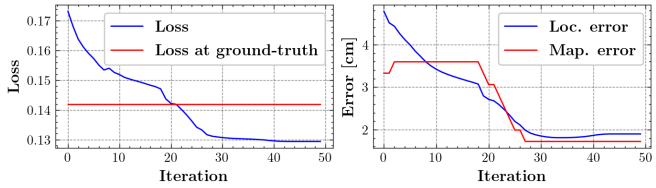

Fig. 9: Evolution of the GraphSLAM cost (left), the localization and mapping errors (right) during the NLS optimization when using the data from Scenario 2.

errors. After convergence, the trajectory is seemingly well estimated, as shown in Fig 7d. Fig. 8 shows the evolution of the loss, the localization error, defined as the average error of the estimated positions in the plate frame, and the mapping error, defined as the average error on the plate dimensions. One can see that the optimization process is efficient, as the loss is substantially decreased until it becomes lower than the loss evaluated at the ground-truth. Also, the localization error is sensibly reduced, while the mapping error is slightly decreased. After convergence, both localization and mapping accuracies are better than 1cm.

We run the same experiment for Scenario 2, and Fig. 9 shows the results of the optimization. One can see that both localization and mapping errors are sensibly reduced, until the accuracies become better than 2cm. To assess the repeatability of our approach, we run it again 10 times in each of the two scenarios, and randomly generate the noisy odometry data. Table I shows the localization and mapping errors, both at initialization and after convergence. One can see that the achieved levels of accuracy remain consistent.

V. CONCLUSIONS

This paper presents a framework to solve the full SLAM problem for an inspection robot relying on UGWs on a metal surface. An observation model that can leverage multi-order echoes is integrated, along with beamforming, within a standard NLS optimizer. Experimental results show that the designed observation model yields better localization accuracy than a first-order echo model, and the proposed GraphSLAM framework can achieve SLAM results with centimeter accuracy, in a laboratory environment. In future works, the proposed framework shall be further evaluated in more realistic scenarios. Besides, a Non-Gaussian SLAM approach, as in [16], could be integrated to better take into account the uncertainty induced by the use of beamforming. Last, other map features such as defects shall be included in the map for a complete inspection task.

REFERENCES

[1] G. Dobie, S. G. Pierce, and G. Hayward, "The feasibility of synthetic aperture guided wave imaging to a mobile sensor platform," *Ndt & E International*, vol. 58, pp. 10–17, 2013.

[2] Z. Su and L. Ye, *Identification of damage using Lamb waves: from fundamentals to applications*. Springer Science & Business Media, 2009, vol. 48.

[3] S. Thrun, W. Burgard, D. Fox *et al.*, *Probabilistic robotics, vol. 1*. MIT press Cambridge, 2005.

[4] G. Grisetti, R. Kümmerle, C. Stachniss, and W. Burgard, "A tutorial on graph-based slam," *IEEE Intelligent Transportation Systems Magazine*, vol. 2, no. 4, pp. 31–43, 2010.

[5] H. Lamb, "On waves in an elastic plate," *Proceedings of the Royal Society of London. Series A, Containing papers of a mathematical and physical character*, vol. 93, no. 648, pp. 114–128, 1917.

[6] O. L. Ouabi, P. Pomarede, M. Geist, N. F. Declercq, and C. Pradalier, "A FastSLAM Approach Integrating Beamforming Maps for Ultrasound-Based Robotic Inspection of Metal Structures," *IEEE Robotics and Automation Letters*, vol. 6, no. 2, pp. 2908–2913, 2021.

[7] B. D. Van Veen and K. M. Buckley, "Beamforming: a versatile approach to spatial filtering," *IEEE ASSP Magazine*, 1988.

[8] Z. Su, L. Ye, and Y. Lu, "Guided lamb waves for identification of damage in composite structures: A review," *Journal of sound and vibration*, vol. 295, no. 3-5, pp. 753–780, 2006.

[9] R. Enjikalayil Abdulkader, P. Veerajagadheswar, N. Htet Lin, S. Kumaran, S. R. Vishaal, and R. E. Mohan, "Sparrow: A magnetic climbing robot for autonomous thickness measurement in ship hull maintenance," *Journal of Marine Science and Engineering*, vol. 8, no. 6, p. 469, 2020.

[10] C. Gonzales, A. Balyan, M. Mallari, and C. Schaal, "Lamb wave-based nondestructive inspection using a mobile robotic platform," in *Health Monitoring of Structural and Biological Systems XV*, vol. 11593. International Society for Optics and Photonics, 2021, p. 115932V.

[11] R. Kümmerle, G. Grisetti, H. Strasdat, K. Konolige, and W. Burgard, "g 2 o: A general framework for graph optimization," in *2011 IEEE International Conference on Robotics and Automation*. IEEE, 2011, pp. 3607–3613.

[12] M. Kaess, A. Ranganathan, and F. Dellaert, "isam: Incremental smoothing and mapping," *IEEE Transactions on Robotics*, vol. 24, no. 6, pp. 1365–1378, 2008.

[13] M. Kaess, H. Johannsson, R. Roberts, V. Ila, J. J. Leonard, and F. Dellaert, "isam2: Incremental smoothing and mapping using the bayes tree," *The International Journal of Robotics Research*, vol. 31, no. 2, pp. 216–235, 2012.

[14] F. Herranz, Á. Llamazares, E. Molinos, and M. Ocaña, "A comparison of slam algorithms with range only sensors," in *2014 IEEE International Conference on Robotics and Automation (ICRA)*. IEEE, 2014, pp. 4606–4611.

[15] A. Arun, R. Ayyalasomayajula, W. Hunter, and D. Bharadia, "P2slam: Bearing based wifi slam for indoor robots," *IEEE Robotics and Automation Letters*, vol. 7, no. 2, pp. 3326–3333, 2022.

[16] M. Y. Cheung, D. Fourie, N. R. Rypkema, P. V. Teixeira, H. Schmidt, and J. Leonard, "Non-gaussian slam utilizing synthetic aperture sonar," in *2019 International Conference on Robotics and Automation (ICRA)*. IEEE, 2019, pp. 3457–3463.

[17] E. Leitinger, F. Meyer, F. Hlawatsch, K. Witrisal, F. Tufvesson, and M. Z. Win, "A belief propagation algorithm for multipath-based slam," *IEEE transactions on wireless communications*, vol. 18, no. 12, pp. 5613–5629, 2019.

[18] M. Kreković, I. Dokmanić, and M. Vetterli, "Echoslam: Simultaneous localization and mapping with acoustic echoes," in *2016 IEEE International Conference on Acoustics, Speech and Signal Processing (ICASSP)*. Ieee, 2016, pp. 11–15.

[19] I. Dokmanić, L. Daudet, and M. Vetterli, "From acoustic room reconstruction to slam," in *2016 IEEE International Conference on Acoustics, Speech and Signal Processing (ICASSP)*. Ieee, 2016, pp. 6345–6349.

[20] M. Kreković, I. Dokmanić, and M. Vetterli, "Omnidirectional bats, point-to-plane distances, and the price of uniqueness," in *2017 IEEE International Conference on Acoustics, Speech and Signal Processing (ICASSP)*. Ieee, 2017, pp. 3261–3265.

[21] R. Worley, Y. Yu, and S. Anderson, "Acoustic echo-localization for pipe inspection robots," in *2020 IEEE International Conference on Multisensor Fusion and Integration for Intelligent Systems (MFI)*. IEEE, 2020, pp. 160–165.

[22] C. Pradalier, O.-L. Ouabi, P. Pomarede, and J. Steckel, "On-plate localization and mapping for an inspection robot using ultrasonic guided waves: a proof of concept," in *IROS*. IEEE, 2020.

[23] H. Kuttruff, *Room acoustics*. Crc Press, 2016.

[24] J. B. Allen and D. A. Berkley, "Image method for efficiently simulating small-room acoustics," *The Journal of the Acoustical Society of America*, vol. 65, no. 4, pp. 943–950, 1979.

[25] O.-L. Ouabi, J. Yi, N. Zeghidour, N. Declercq, M. Geist, and C. Pradalier, "Polygonal shapes reconstruction from acoustic echoes using a mobile sensor and beamforming," 2022.

[26] A. R. Curtis, M. J. Powell, and J. K. Reid, "On the estimation of sparse jacobian matrices," *J. Inst. Math. Appl*, vol. 13, no. 1, pp. 117–120, 1974.